Chemical Science

ROYAL SOCIETY OF CHEMISTRY

EDGE ARTICLE

View Article Online
View Journal | View Issue

Check for updates

Cite this: *Chem. Sci.*, 2025, **16**, 418

All publication charges for this article have been paid for by the Royal Society of Chemistry

Received 18th September 2024
Accepted 22nd November 2024

DOI: 10.1039/d4sc06323f

rsc.li/chemical-science

Spatially confined transition metals boost high initial coulombic efficiency in alloy anodes†

Haoyu Fu, ‡[a] Fangchao Gu,‡[a] Yize Niu,‡[a] Shuxuan Liao,[a] Zeyuan Bu,[a] Haonan Wang,[a] Dong Yang,[a] Xiaoshan Wang*[a] and Qiang Li *[ab]

Alloy-type materials hold significant promise as high energy density anodes for lithium-ion batteries. However, the initial coulombic efficiency (ICE) is significantly hindered by the poor reversibility of the conversion reaction and volume expansion. Here, the NiO/SnO_2 multilayers with a hybrid interface of alloy and transition metal oxides are proposed to generate Ni nanoparticles within confined layers, catalyzing Li_2O decomposition and suppressing the coarsening of Sn or Li_2O particles. Supported by density functional theory (DFT) calculations and revealed by *operando* magnetometry, the spatially confined, well maintained Ni active sites lower the energy barrier for Li–O bond rupture and enhance the migration dynamics of Li^+. The enhanced reaction kinetics lead to achievement of an impressive ICE of 92.3% and a large capacity of 1247 mA h g^{-1} with 97% retention after 800 cycles. Furthermore, the NiO/SnO_2 anode exhibits excellent electrochemical performances in both Na/K-ion batteries. Notably, when constructed with the same framework, SiO_2 also delivers significantly improved lithium storage properties with ultra-high ICEs. This work paves the way for advanced designs of alloy-type anodes that satisfy both ICE and overall electrochemical performance.

Open Access Article. Published on 02 December 2024. Downloaded on 1/15/2026 8:13:41 PM.
This article is licensed under a Creative Commons Attribution-NonCommercial 3.0 Unported Licence.

Introduction

The rapid growth of new energy vehicles and large-scale energy storage systems has increased the demand for energy storage devices with lithium-ion batteries (LIBs) bearing the majority of this demand.[1–3] Among well-studied LIB anode materials, alloy-type materials (*e.g.*, Sn, Si, Ge, *etc.*) based on alloying/de-alloying reactions have emerged as a promising candidate anode alongside commercial graphite materials due to their high theoretical capacity, low working potential and cost-effectiveness.[4–11] These alloy-type anodes typically suffer from drastic volume expansion (>300%), leading to poor electronic/ion conductivity, continuous growth of the solid electrolyte interphase (SEI), and significant performance degradation.[12–14] Recently, MO_x anodes (M = Sn, Si, *etc.*) have played a crucial role in advancing energy storage solutions and often exhibit better cycling stability, as the Li_2O matrix generated from the conversion reaction ($xLi^+ + MO_x + xe^- \rightarrow M + xLi_2O$) alleviates expansion stress and reduces volume fluctuations.[15–17] However, the poor reversibility of the conversion reaction results in low initial coulombic efficiency (ICE), a critical factor for anode materials as it dictates the ability to mitigate irreversible capacity loss.[18] A low ICE reduces energy density of a battery, significantly limiting its practical applicability.[19] Therefore, improving the ICE of alloy-type anodes is essential for successful commercial implementation.

Two main factors have been identified as the primary determinants of low ICE in alloy-type anodes. First, as discussed above, the irreversible transformation of Li_2O results in poor reversibility for the conversion reaction.[20,21] Meanwhile, the volume expansion of M (*e.g.*, Sn and Si) during the alloying reaction causes continuous SEI growth, ultimately leading to partial lithium depletion.[18] To achieve a high ICE, researchers have attempted to reduce the electrode size and enhance the contact area between M and Li_2O.[22,23] For example, Park *et al.* proposed high-entropy silicon anodes by the element screening method, facilitating mass and charge transport and achieving a high ICE of 90.3%.[24,25] Li *et al.* synthesized alloy anodes with a disordered lattice and liquid metal phase to achieve higher metallic conductivity, improving the ICE up to 91%.[26] However, the ongoing coarsening of grains, along with the associated volume expansion and electrode fractures, further accelerates the capacity decay. Additionally, transition metals (TMs) could catalyze the decomposition of Li_2O and facilitate the phase transition, and are commonly utilized in the construction of alloy-type anodes. However, building alloy-type anodes with small-sized, highly active TMs to achieve an ICE over 90% remains challenging.[27–31] Early research demonstrated that small-sized, highly active TMs can be generated *in situ* from

[a]*College of Physics, Weihai Innovation Research Institute, College of Materials Science and Engineering, Qingdao University, Qingdao 266071, China. E-mail: wangxiaoshan1@qdu.edu.cn; liqiang@qdu.edu.cn*

[b]*University of Waterloo, Waterloo, Ontario N2L 3G1, Canada*

† Electronic supplementary information (ESI) available. See DOI: https://doi.org/10.1039/d4sc06323f

‡ Co-first-author.

© 2025 The Author(s). Published by the Royal Society of Chemistry

Open Access Article. Published on 02 December 2024. Downloaded on 1/15/2026 8:13:41 PM. This article is licensed under a Creative Commons Attribution-NonCommercial 3.0 Unported Licence.

transition metal oxides (TMOs) during the lithiation process.[17,32] In this context, hybridizing alloy-type metals with TMOs in a confined space may offer a new approach for achieving high ICE.

Herein, we report magnetron-sputtered NiO/SnO_2 multilayers (NSMs) capable of achieving an ultra-high ICE up to 92.3% and a remarkable capacity retention of 97% after 800 cycles. As a self-supporting electrode material, the prepared nanocomposite films have been successfully utilized in quasi-solid state batteries. *Operando* magnetometry tracks the phase evolution during the charge–discharge process. The tightly wrapped nanolayer structure provides a confined space to stabilize reduced Ni particles, suppressing the coarsening of Sn and Li_2O particles. Density functional theory (DFT) calculations revealed that the free energy of Li–O bonds and the migration dynamics of Li^+ are significantly influenced by active Ni nanoparticles (NPs), thus facilitating the subsequent delithiation process of Li_2O. Furthermore, the NiO/SnO_2 anode exhibits decent electrochemical performance in Na/K-ion batteries (SIBs/PIBs), demonstrating great promise as advanced anode materials for next-generation batteries. More interestingly, the superior ICE improvement strategy is universal in NiO/SiO_2, CoO/SnO_2, and Fe_2O_3/SnO_2 alloy-type anode materials.

Results and discussion

The schematic illustration of the NiO/SnO_2 multilayers fabricated by magnetron sputtering is shown in Fig. 1a. Layers of 5 nm NiO and 10 nm SnO_2 are alternately sputtered onto the copper electrode to form well-confined NiO/SnO_2 interfaces. The synthesized multilayer films are directly used as binder-free anodes for lithium-ion batteries (Fig. 1a). All tested film materials and their preparation conditions are summarized in Table S1.† The X-ray diffraction pattern demonstrates the amorphous nature of the NSM (Fig. S1a†), which is further confirmed by the twisted and disordered lattice pattern of NiO and SnO_2 in the corresponding TEM image (Fig. S1b†). The X-ray photoelectron spectroscopy (XPS) survey spectrum of the NSM (Fig. S2a†) confirms the existence of C, O, Sn and Ni. And high-resolution XPS validates the dominant valences states of Ni^{2+} (Fig. S2b†) and Sn^{4+} (Fig. S2c†) in the NSM, representing the original high purity film. The cyclic voltammograms (CVs) of the samples *versus* Li^+/Li recorded in the range of 0–3 V at a scan rate of 0.5 mV s^{-1}, are shown in Fig. 1b. In the first negative scan for NSM, SnO_2 or NiO combined with Li^+ ions shows a reduction peak at around 1.2 V (*i.e.*, $SnO_2 + 4Li^+ + 4e^- \rightarrow Sn + 2Li_2O$ and $NiO + 2Li^+ + 2e^- \rightarrow Ni + Li_2O$, respectively).[33] The cathodic peaks at around 0.55 V and 0.25 V are attributed to the formation of the solid-electrolyte interface (SEI) layer and the alloying reaction ($Sn + xLi^+ + 2e^- \rightarrow Li_xSn$).[33,34] In the first positive scan, the peaks detected at 0.5 V and 2.2 V are attributed to the dealloying of Li_xSn alloys and the oxidation of Ni to NiO, respectively.[35] Notably, the NSM shows stronger decomposition peaks of Li_2O ($Sn + 2Li_2O \rightarrow SnO_2 + 4Li^+ + 4e^-$) compared to pure SnO_2 between 1.0 V and 2.0 V, indicating a significant improvement in the reversibility of the conversion reaction.

The electrochemical performance of the NiO/SnO_2 multilayer electrode was investigated by using coin-type half cells (LIBs). As shown in Fig. 1c, the specific capacities of the NSM anode for the first charge and discharge are 1543.1 and 1671.9 mA h g^{-1} respectively, corresponding to a high initial coulombic efficiency (ICE) of 92.3%, as one of the best SnO_2-based electrode performances reported in the literature (Fig. 1d). In contrast, the ICEs of pure NiO (Fig. S3†) and SnO_2 are only 63.2% and 71.9%, respectively. The rate capability of NSM and SnO_2 electrodes at current rates ranging from 0.5 to 5 A g^{-1} is shown in Fig. 1e. The NSM anode delivers a reversible capacity of 1453.2 mA h g^{-1} at a current density of 1 A g^{-1}. When the current rate returns to 0.5 A g^{-1}, 91.8% of the original capacity (1333.7 mA h g^{-1}) is retained. In contrast, the SnO_2 electrode only exhibits 1038.5 mA h g^{-1} at 1 A g^{-1} and retained only 60.6% of its capacity at 0.5 A g^{-1}. Long-term cycling stability was evaluated at a current density of 1 A g^{-1}.Remarkably, the NSM anode exhibits excellent cycling stability (Fig. 1f) with nearly 100% coulombic efficiency and retains 97% of its reversible specific capacity even after 800 deep cycles.

To further understand the remarkable ICE stemming from the high reversibility of the conversion reaction ($Li_2O + Sn \rightarrow SnO_2 + Li^+$), *ex situ* XPS characterization was conducted at different potentials. As shown in Fig. 2a, when gradually charged to 3 V, Sn^{4+} fully occupies the valence state in the NSM, whereas in bare SnO_2 (Fig. 2b), 17% of Sn remains in the Sn^0 state along with Sn^{4+}.[36] After 50 cycles (Fig. S4†), the Sn^0 content increases to 68% in bare SnO_2 (Fig. S4a†), while the NSM still shows Sn^{4+} without any impurities (Fig. S4b†), indicating Sn and Li_xSn coarsening in bare SnO_2 and the high reversibility of the conversion reaction in the NSM electrode. This result is consistent with the differential charge capacity plots (DCPs) observed in the NSM (Fig. 2c). The shift of the dealloying peak ($Li_xSn \rightarrow Sn$) towards higher potential suggests increasing polarization due to the coarsening of Sn and Li_xSn. Meanwhile, the conversion reaction peaks from 1.0 to 2.0 V disappear after

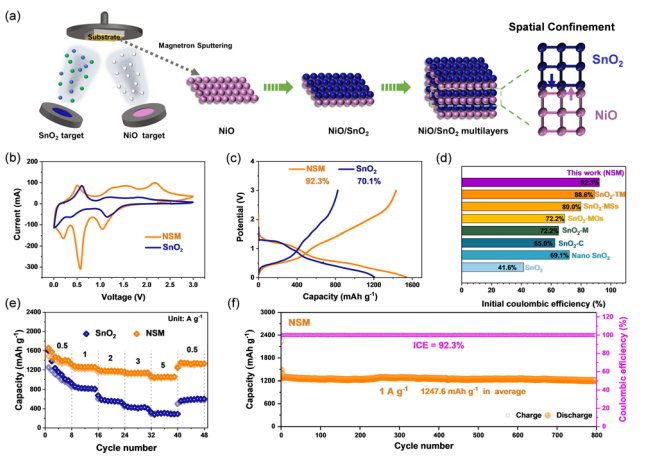

Fig. 1 (a) Schematic illustration of the NSM preparation process. (b) CV curves at 0.5 mV s^{-1} for the first cycle. (c) Initial charge–discharge curves at 1 A g^{-1}. (d) ICE comparison with reported SnO_2-based anodes. (e) Rate performance. (f) Long-term cycle performances at 1 A g^{-1}.

Open Access Article. Published on 02 December 2024. Downloaded on 1/15/2026 8:13:41 PM.
This article is licensed under a Creative Commons Attribution-NonCommercial 3.0 Unported Licence.

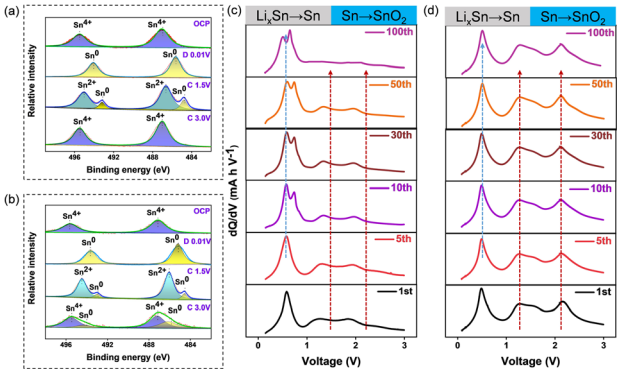

Fig. 2 *Ex situ* XPS spectra of Sn 3d for (a) NSM and (b) SnO_2 at four different charge states. Differential charge capacity *versus* voltage plots for (c) SnO_2 and (d) NSM electrodes from the 1st to the 100th cycles.

100 cycles in bare SnO_2, indicating the failure of conversion reaction reversibility. Notably, the dealloying peak of the NSM remains stable even after 100 cycles (Fig. 2d), confirming the high reversibility and stability of the conversion/alloying reaction.[37,38]

To explore the underlying reaction mechanism of the highly reversible and stable conversion reactions in the NSM structure,

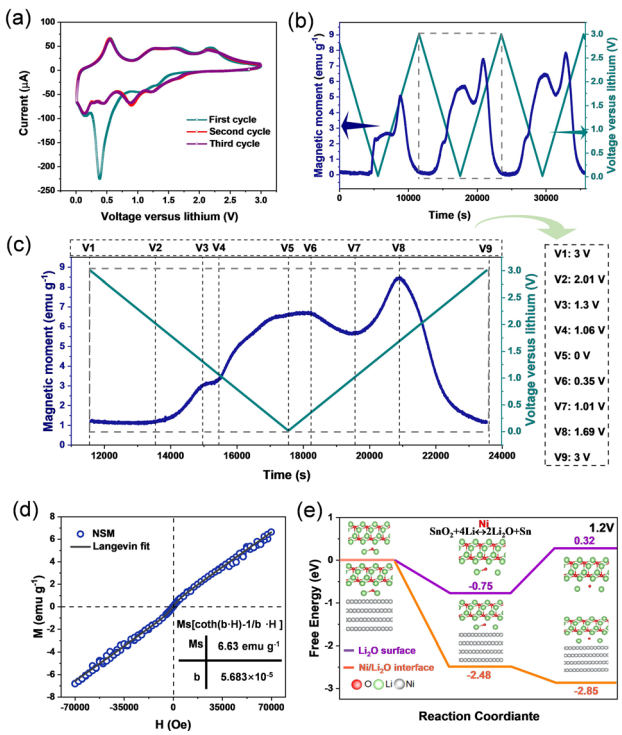

Fig. 3 Analysis of the reaction mechanism of the NSM anode in LIBs using *operando* magnetometry. (a) CV curves for the first three cycles at a scan rate of 0.5 mV s^{-1} over a potential window from 0.01 V to 3 V. (b) *Operando* magnetic monitoring as a function of CV scanning under an applied magnetic field of 3*T*, and (c) the corresponding magnified view of the dotted area. (d) Langevin fitting curve for the hysteresis loop at a charge of 1.0 V. (e) Free energy for breaking Li–O bonds at the Ni/Li_2O interface and Li_2O surface at 1.2 V.

the phase evolution process during cycling was investigated using *operando* magnetometry.[39–44] Fig. 3a and b show CV curves and time-sequenced magnetization of the NSM electrode, along with the potential response during the first three cycles. The periodic magnetization variation reflects the reversible and steady electrochemical processes. The second discharge/charge cycle response is magnified and discussed in detail (Fig. 3c). The peaks and valleys at different voltages in the real-time magnetization variation are labeled as V1 to V9. The lack of magnetization variation indicates that no reaction of NiO occurs from V1 to V2. The pronounced increase in magnetization from V2 to V3 is likely due to the reduction from NiO to Ni. The metallic Ni^0 continues to store spin-polarized electrons between V3 and V4, thereby reducing the slope of the magnetization increase.[45,46] Followed by the formation and decomposition of the SEI, the magnetization increases (V4 to V5) and then falls (V6 to V7) corresponding to electron transfer.[47] As spin-polarized electrons are released from metallic Ni^0, a significant increase in magnetization occurs from V7 to V8. The oxidation from Ni to NiO from V8 to V9 induces a rapid decline in magnetization. Thus, the *in situ* phase evolution of Ni particles in the lithiation process is successfully described by the advanced *operando* monitoring magnetization, addressing the limitations of the *ex situ* technique.[29,35,48] The size of Ni particles was later quantified using Langevin fitting, as shown in Fig. 3d. The fitted curve matches perfectly with the experimental data, and the calculated diameter of the Ni particle is 1.2 nm. The result proves that the confined multilayers restrict the Ni particle size to the nanoscale, ensuring their uniform dispersion in layers, which provides more electron transport channels. Furthermore, DFT calculations (Fig. 3e) were used to investigate the relationship between Ni NPs and the decomposition of inactive Li_2O at a potential of 1.2 V. As shown in Fig. 3e, the Li–O bond breaking process at the Ni/Li_2O interface is an exothermic reaction with a total free energy of −2.85 eV, while the Li_2O interface exhibits an energy barrier of 1.07 eV. This confirms that the Ni NPs accelerate the delithiation of Li_2O, consistent with the highly reversible conversion reactions in the NSM.

The overall morphology and surface microstructure of NSM and SnO_2 electrodes were examined after 50 discharge–charge cycles. In the SEM image, the SnO_2 electrode exhibits significant volume expansion and a fractured surface (Fig. S5a†). The corresponding staggered lattices observed in STEM (Fig. S6a and b†) are identified as unreacted Sn, SnO_2 and Li_2O particles. In contrast, the NSM electrode (Fig. S5b†), comprising SnO_2 and NiO composites, largely maintains its original structure with minimal changes (Fig. S6d and e†).[49] EDX mappings show a uniform distribution of C, O and Sn elements in the NSM electrode after 50 cycles, suggesting no significant atom migration or aggregation during the cycling process. In contrast, the SnO_2 electrode shows evident particle aggregation due to the poor distribution of Sn (Fig. S7†).[50] Overall, these observations strongly support our experimental results, such as those of *operando* magnetometry, validating the reversible structural transformation catalysed by Ni NPs in the NSM electrode. Additionally, compared with the thicker SEI film in

© 2025 The Author(s). Published by the Royal Society of Chemistry

Open Access Article. Published on 02 December 2024. Downloaded on 1/15/2026 8:13:41 PM. This article is licensed under a Creative Commons Attribution-NonCommercial 3.0 Unported Licence.

the SnO_2 electrode (Fig. S6c†), the NSM electrode possesses a more uniform SEI film (Fig. S6f†), which reduces the impact of electrolyte corrosion and surface side reactions. Thus, such a synergistic interaction between the internal reversible structure and external SEI protection significantly improves both the cycle stability and rate performance.

The kinetic behavior of a lithium-ion battery in the whole cycle was investigated using the galvanostatic intermittent titration technique (GITT) method (Fig. 4a).[4,51] The diffusion coefficient (log *D*) of the NSM is significantly higher than that of SnO_2, indicating a faster ion diffusion rate. Electrochemical impedance spectroscopy (EIS) was used to detect changes in internal resistance during the electrochemical process. Fig. 4b illustrates the impedance from the 1st to the 200th cycles. Notably, by the 100th cycle, the impedance of the SnO_2 electrode increased fourfold compared to the initial cycle (Table S2†). This drastic rise indicates the electrode's failure to maintain structural integrity due to Li_2O deposition and Sn particle agglomeration during the process (Fig. S8†).[52] Conversely, the impedance of the NSM shows minimal change even after 200 cycles, implying high structure reversibility during the reaction. For detailed insights, we conducted EIS of both NSM and SnO_2 electrodes in the alloying/dealloying voltage range and during the decomposition of Li_2O (discharge to 0.25 V and charged to 0.5 V, 1.2 V or 1.8 V, respectively) in a single cycle (Fig. 4c). The equivalent circuit fitting is shown in Fig. S9.† The NSM electrode exhibits lower charge transfer resistance (R_{ct}) in smaller semicircles at high-to-medium frequencies and various potentials compared to bare SnO_2, suggesting superior electrical conductivity of the NSM electrode.[4] The density of states (DOS) curves further emphasize the conductivity difference between SnO_2 and the NSM (Fig. 4d and e). Above the conduction band, the DOS intensity of the NSM is much higher than that of SnO_2, indicating a lower energy demand for the electron transition in the NSM, which corresponds to higher conductivity.[53] These results demonstrate that the NSM structure significantly enhances Li^+ diffusion and charge transfer, thereby markedly improving rate performance.

The schematic diagram of the high electrochemical performance mechanism, particularly in achieving ultra-high ICE for the NSM configuration, is summarized as follows (Fig. 5a): (1) Ni nanoparticles are first *in situ* generated from NiO and widely distributed in SnO_2 multilayers to catalyze the decomposition of Li_2O and promote the conversion reaction from Sn/Li_2O to SnO_2. (2) The multilayer structure effectively stabilizes Ni NP active sites and inhibits the coarsening of Sn and Li_2O particles by creating a confined environment. Additionally, it prevents the formation of a thicker and uneven SEI layer, thereby alleviating volume expansion. (3) The nanosized Ni particles derived from the well-designed NSM provide more electron transport channels and facilitate Li^+ diffusion and charge transfer, thereby elevating reaction kinetics. The same strategy has been extended to NiO/SiO_2, CoO/SnO_2 and Fe_2O_3/SnO_2 multilayers to explore their applicability and effectiveness in lithium batteries, as shown in Fig. S10–S14.† It is found that the nanostructure NiO/SiO_2 electrode exhibits excellent comprehensive electrochemical performance, achieving an ultrahigh average ICE of 81.2%, significantly surpassing that of pure SiO_2. Additionally, the CoO/SnO_2 and Fe_2O_3/SnO_2-based electrodes also exhibited remarkable performance, delivering an ultrahigh ICE of 91.1% and 90.5% at 500 mA g^{-1}, with high capacities and rate performance, respectively. Moreover, leveraging the structural benefits, the NSM electrode achieves one of the best electrochemical performances reported for sodium-ion batteries (SIBs) and potassium-ion batteries (PIBs), (Fig. S15 to S17; see the ESI† for details). The flexibility and adaptability of this structure make it suitable for various types of batteries, including lithium-ion, sodium-ion, or potassium-ion batteries, enabling outstanding performance across different applications.

To evaluate the practical application prospects of the NSM, quasi-solid-state pouch flexible cells (NSM|P(VDF-HFP)|$LiCoO_2$) were assembled as shown in Fig. 5b.[54,55] The full

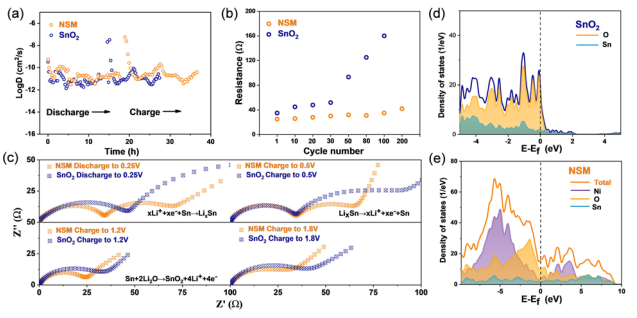

Fig. 4 Kinetic analysis of the electrochemical behavior of SnO_2 and NSM electrodes. (a) GITT analysis of SnO_2 and the NSM. (b) Impedance at different cycles. (c) Electrochemical impedance spectroscopy (EIS) of SnO_2 and NSM electrodes at discharge to 0.25 V, charge to 0.5 V, charge to 1.2 V and charge to 1.8 V. (d) DOS curves of the SnO_2 model and (e) the NSM model.

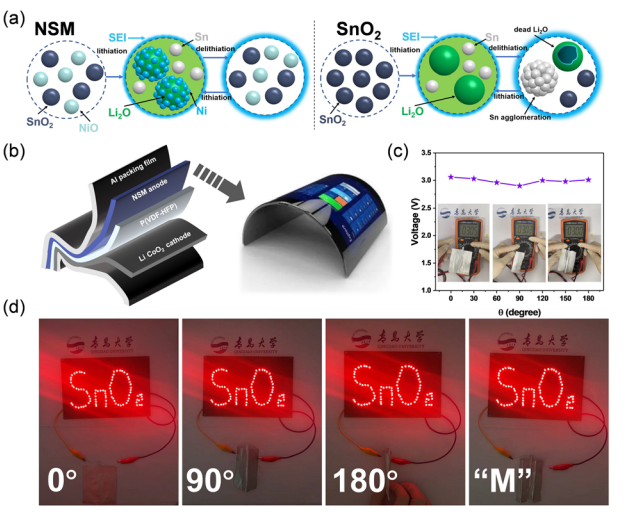

Fig. 5 (a) Schematic diagram of the electrochemical performance mechanism of NSM and SnO_2 electrodes. (b) Structure model of a thin film battery and photographs of an electrochromic watch powered by a flexible battery. (c) Open circuit voltage and (d) an LED logo of SnO_2 powered by a flexible quasi-solid-state pouch cell at varied folding levels.

Open Access Article. Published on 02 December 2024. Downloaded on 1/15/2026 8:13:41 PM. This article is licensed under a Creative Commons Attribution-NonCommercial 3.0 Unported Licence.

battery features an equal size 40 mm cathode and anode. The open circuit voltage of the battery device remains almost unchanged (approximately 3.0 V) at different folding states (Fig. 5c). As another demonstration, a "SnO_2" logo comprising 90 LEDs is well illuminated by the flexible battery in both flat and various bending states (Fig. 5d). These electrochemical measurements highlight the key characteristics of flexibility and adaptability, providing a continuous and stable power supply despite changes in its physical shape or bending states. We also assembled coin-type full cells with the NSM and $LiNi_{0.8}Co_{0.1}Mn_{0.1}O_2$ as the anode and cathode separately, demonstrating similarities in the ultra-high capacity and ICE (Fig. S18†). On this basis, the "small and powerful" flexible battery is expected to be a competitive candidate for energy storage and conversion components in next-generation microelectronic devices, as well as in future integrated electronic devices.

Conclusion

In summary, a NiO/SnO_2 multilayer anode with confined transition metal oxide (TMO) layers has been developed for Li-ion batteries using an alternating magnetron sputtering method. The designed hierarchical structure of the NSM exhibits an ultrahigh ICE of 92.3% and a large capacity of 1247.6 mA h g^{-1}, retaining ~97% after 800 cycles. *Operando* magnetometry directly evidences the evolution of Ni NPs from NiO, and the DFT calculations revealed that the Ni NPs significantly lower the energy barrier for breaking Li–O bonds, thereby facilitating the conversion reaction from Sn/Li_2O to SnO_2. Additionally, the confined environment in the NSM helps inhibit the coarsening of Sn and Li_2O by maintaining the nanoscale of Ni active sites, effectively alleviating volume expansion. Moreover, the well-dispersed Ni NPs profoundly enhance the conductivity and reaction kinetics by providing more electron transport channels and shortening the diffusion distance of Li^+ and electrons, respectively. As expected, in a broader range of interfacial systems, we found that NiO/SiO_2, CoO/SnO_2, and Fe_2O_3/SnO_2 anodes all show significant performance improvements with an ultrahigh ICE of 81.2%, 91.1% and 90.5%, respectively. The multifunctionality and universality of NiO/SnO_2 anodes in Na/K-ion batteries and flexible quasi-solid-state full cells highlight their widespread feasibility, offering a promising path towards high-performance energy storage solutions.

Data availability

Essential data are provided in the main text and the ESI.† Additional data are available from the authors upon reasonable request.

Author contributions

H. Y. Fu: conceptualization, data curation, formal analysis, investigation, methodology, validation, visualization, writing – original draft. F. C. Gu: conceptualization, data curation, formal analysis, investigation, methodology, validation, visualization. Y. Z. Niu, S. X. Liao, Z. Y. Bu, H. N. Wang, and D. Yang: data curation, formal analysis, investigation, visualization. X. S. Wang: funding acquisition, supervision, writing – review & editing. Q. Li: funding acquisition, project administration, resources, supervision, writing – review & editing.

Conflicts of interest

There are no conflicts to declare.

Acknowledgements

This work was supported by the National Natural Science Foundation of China (22179066, 92372127 and 22408192), the Natural Science Foundation of Shandong Province (ZR202210060028), the Postdoctoral Fellowship Program of CPSF under Grant GZC20231188, and the Shandong post-doctoral innovation program (SDCX-ZG-202400262).

Notes and references

1 L. L. Hu, M. H. Jin, Z. Zhang, H. X. Chen, F. B. Ajdari and J. X. Song, Interface-adaptive binder enabled by supramolecular interactions for high-capacity Si/C composite anodes in lithium-ion batteries, *Adv. Funct. Mater.*, 2022, **32**, 2111560.

2 S. Chae, S. H. Choi, N. Kim, J. Sung and J. Cho, Integration of graphite and silicon anodes for the commercialization of high-energy lithium-ion batteries, *Angew. Chem., Int. Ed.*, 2020, **59**, 110–135.

3 Y. S. Zhu, C. T. Wang, Z. J. Cheng, Q. Yao, J. Su, B. Chen, J. Yang and Y. T. Qian, Bimetallic Bi-Sn microspheres as high initial coulombic efficiency and long lifespan anodes for sodium-ion batteries, *Chem. Commun.*, 2022, **58**, 5140–5143.

4 S. Y. Pan, J. W. Han, Y. Q. Wang, Z. S. Li, F. Q. Chen, Y. Guo, Z. S. Han, K. F. Xiao, Z. C. Yu, M. Y. Yu, S. C. Wu, D. W. Wang and Q. H. Yang, Integrating SEI into layered conductive polymer coatings for ultrastable silicon anodes, *Adv. Mater.*, 2022, **34**, 2203617.

5 M. Q. Peng, K. Shin, L. X. Jiang, Y. Jin, K. Zeng, X. L. Zhou and Y. B. Tang, Alloy-type anodes for high-performance rechargeable batteries, *Angew. Chem., Int. Ed.*, 2022, **61**, e202206770.

6 X. W. Zhou, T. Y. Li, Y. Cui, M. L. Meyerson, J. A. Weeks, C. B. Mullins, Y. Jin, Y. Z. Liu and L. K. Zhu, In situ and operando morphology study of germanium-selenium alloy anode for lithium-ion batteries, *ACS Appl. Energy Mater.*, 2020, **3**, 6115–6120.

7 M. Chen, P. Xiao, K. Yang, B. X. Dong, D. Xu, C. Y. Yan, X. J. Liu, J. T. Zai, C. J. Low and X. F. Qian, Sn anodes protected by intermetallic $FeSn_2$ layers for long-lifespan sodium-ion batteries with high initial coulombic efficiency of 93.8%, *Angew. Chem., Int. Ed.*, 2023, **62**, e202219177.

8 H. Zhang, K. Tao, X. Zeng, C. Chen, Y. Zhu, T. Han, J. Li and J. Liu, Rationally engineering a binary $SnS_{0.5}Se_{0.5}$/carbon

© 2025 The Author(s). Published by the Royal Society of Chemistry

Open Access Article. Published on 02 December 2024. Downloaded on 1/15/2026 8:13:41 PM. This article is licensed under a Creative Commons Attribution-NonCommercial 3.0 Unported Licence.

nest-coated Si nanosphere for a high-performance lithium-ion battery anode, *Chem. Sci.*, 2024, **15**, 15769–15775.

9 M. F. Hassan, M. M. Rahman, Z. Guo, Z. Chen and H. Liu, SnO_2-NiO-C nanocomposite as a high capacity anode material for lithium-ion batteries, *J. Mater. Chem.*, 2010, **20**, 9707–9712.

10 Y. Li, C. Ou, J. Zhu, Z. Liu, J. Yu, W. Li, H. Zhang, Q. Zhang and Z. Guo, Ultrahigh and durable volumetric lithium/sodium storage enabled by a highly dense graphene-encapsulated nitrogen-doped carbon@Sn compact monolith, *Nano Lett.*, 2020, **20**, 2034–2046.

11 K. Duan, J. Ning, L. Zhou, S. Wang, Q. Wang, J. Liu and Z. Guo, Synergistic inorganic-organic dual-additive electrolytes enable practical high-voltage lithium-ion batteries, *ACS Appl. Mater. Interfaces*, 2022, **14**, 10447–10456.

12 L. Tan, X. X. Lan, J. W. Chen, H. Y. Zhang, R. Z. Hu and M. Zhu, LiF-induced stable solid electrolyte interphase for a wide temperature SnO_2-based anode extensible to -50 °C, *Adv. Energy Mater.*, 2021, **11**, 2101855.

13 Y. Z. Jiang, Y. Li, P. Zhou, Z. Y. Lan, Y. H. Lu, C. Wu and M. Yan, Ultrafast, highly reversible, and cycle-stable lithium storage boosted by pseudocapacitance in Sn-based alloying anodes, *Adv. Mater.*, 2017, **29**, 1606499.

14 S. Park, S. Kim, J.-A. Lee, M. Ue and N.-S. Choi, Liquid electrolyte chemistries for solid electrolyte interphase construction on silicon and lithium-metal anodes, *Chem. Sci.*, 2023, **14**, 9996–10024.

15 N. Nitta, F. X. Wu, J. T. Lee and G. Yushin, Li-ion battery materials: present and future, *Mater. Today*, 2015, **18**, 252–264.

16 L. Zhang, H. B. Wu and X. W. Lou, Growth of SnO_2 nanosheet arrays on various conductive substrates as integrated electrodes for lithium-ion batteries, *Mater. Horiz.*, 2014, **1**, 133–138.

17 R. Z. Hu, D. C. Chen, G. Waller, Y. P. Ouyang, Y. Chen, B. T. Zhao, B. Rainwater, C. H. Yang, M. Zhu and M. L. Liu, Dramatically enhanced reversibility of Li_2O in SnO_2-based electrodes: the effect of nanostructure on high initial reversible capacity, *Energy Environ. Sci.*, 2016, **9**, 595–603.

18 L. Sun, Y. X. Liu, J. Wu, R. Shao, R. Y. Jiang, Z. X. Tie and Z. Jin, A review on recent advances for boosting initial coulombic efficiency of silicon anodic lithium ion batteries, *Small*, 2022, **18**, 2102894.

19 Y. H. Wan, K. M. Song, W. H. Chen, C. D. Qin, X. X. Zhang, J. Y. Zhang, H. L. Dai, Z. Hu, P. F. Yan, C. T. Liu, S. H. Sun, S. L. Chou and C. Y. Shen, Ultra-high initial coulombic efficiency induced by interface engineering enables rapid, stable sodium storage, *Angew. Chem., Int. Ed.*, 2021, **60**, 11481–11486.

20 H. J. Ying, T. T. Yang, P. F. Huang, Z. Zhang, S. L. Zhang, Z. H. Zhang and W. Q. Han, Facile synthesis of hybrid anodes with enhanced lithium-storage performance realized by a "Synergistic Effect", *ACS Appl. Mater. Interfaces*, 2022, **14**, 35769–35779.

21 J. S. Corsi, S. S. Welborn, E. A. Stach and E. Detsi, Insights into the degradation mechanism of nanoporous alloy-type Li-ion battery anodes, *ACS Energy Lett.*, 2021, **6**, 1749–1756.

22 L. Zhang, J. Pu, Y. H. Jiang, Z. H. Shen, J. C. Li, J. Y. Liu, H. X. Ma, J. J. Niu and H. G. Zhang, Low interface energies tune the electrochemical reversibility of tin oxide composite nanoframes as lithium-ion battery anodes, *ACS Appl. Mater. Interfaces*, 2018, **10**, 36892–36901.

23 J. Y. Wang, L. Liao, H. R. Lee, F. F. Shi, W. Huang, J. Zhao, A. Pei, J. Tang, X. L. Zheng, W. Chen and Y. Cui, Surface-engineered mesoporous silicon microparticles as high-Coulombic-efficiency anodes for lithium-ion batteries, *Nano Energy*, 2019, **61**, 404–410.

24 W. Li, Y. Li, J.-H. Wang, S. Huang, A. Chen, L. Yang, J. Chen, L. He, W. K. Pang, L. Thomsen, B. Cowie, P. Xiong, Y. Zhou, G. Jang, D. H. Min, J. S. Byun, L. Xu, J.-Q. Huang, K. C. Roh, S. H. Kang, M. Liu, X. Duan and H. S. Park, Generic synthesis of high-entropy phosphides for fast and stable Li-ion storage, *Energy Environ. Sci.*, 2024, **17**, 5387–5398.

25 W. Li, J.-H. Wang, Y. Li, H. Hsueh, X. Liu, Y. Zhao, S. Huang, X. Li, H.-M. Cheng, X. Duan and H. S. Park, Element Screening of High-Entropy Silicon Anodes for Superior Li-Storage Performance of Li-Ion Batteries, *J. Am. Chem. Soc.*, 2024, **146**, 21320–21334.

26 Y. Li, L. Zhang, H.-Y. Yen, Y. Zhou, G. Jang, S. Yuan, J.-H. Wang, P. Xiong, M. Liu, H. S. Park and W. Li, Single-Phase Ternary Compounds with a Disordered Lattice and Liquid Metal Phase for High-Performance Li-Ion Battery Anodes, *Nano-Micro Lett.*, 2023, **15**, 63.

27 Y. Li, S. L. Yu, T. Z. Yuan, M. Yan and Y. Z. Jiang, Rational design of metal oxide nanocomposite anodes for advanced lithium ion batteries, *J. Power Sources*, 2015, **282**, 1–8.

28 X. H. Wu, W. W. Wu, Y. Zhou, X. S. Huang, W. Chen and Q. Wang, Synthesis and electrochemical performance of SnO_2-Fe_2O_3 composite as an anode material for Na-ion and Li-ion batteries, *Powder Technol.*, 2015, **280**, 119–123.

29 C. X. Hua, X. P. Fang, Z. X. Wang and L. Q. Chen, Transition-metal-catalyzed oxidation of metallic Sn in NiO/SnO_2 nanocomposite, *Chem.–Eur. J.*, 2014, **20**, 5487–5491.

30 J. Choi, W. S. Kim and S. H. Hong, Highly stable SnO_2-Fe_2O_3-C hollow spheres for reversible lithium storage with extremely long cycle life, *Nanoscale*, 2018, **10**, 4370–4376.

31 R. Z. Hu, Y. P. Ouyang, T. Liang, H. Wang, J. Liu, J. Chen, C. H. Yang, L. C. Yang and M. Zhu, Stabilizing the nanostructure of SnO2 anodes by transition metals: a route to achieve high initial coulombic efficiency and stable capacities for lithium storage, *Adv. Mater.*, 2017, **29**, 1605006.

32 W. Wang, J. W. Qin, Z. G. Yin and M. H. Cao, Achieving fully reversible conversion in MoO_3 for lithium ion batteries by rational introduction of $CoMoO_4$, *ACS Nano*, 2016, **10**, 10106–10116.

33 C. H. Chen, P. J. Perdomo, M. Fernandez, A. Barbeito and C. L. Wang, Porous NiO/graphene composite thin films as high performance anodes for lithium-ion batteries, *J. Energy Storage*, 2016, **8**, 198–204.

Open Access Article. Published on 02 December 2024. Downloaded on 1/15/2026 8:13:41 PM. This article is licensed under a Creative Commons Attribution-NonCommercial 3.0 Unported Licence.

34 Y. Z. Jiang, Y. Li, P. Zhou, S. L. Yu, W. P. Sun and S. X. Dou, Enhanced reaction kinetics and structure integrity of Ni/SnO_2 nanocluster toward high-performance lithium storage, *ACS Appl. Mater. Interfaces*, 2015, **7**, 26367–26373.

35 C. Kim, J. W. Jung, K. R. Yoon, D. Y. Youn, S. Park and I. D. Kim, A high-capacity and long-cycle-life lithium ion battery anode architecture: silver nanoparticle-decorated SnO_2/NiO nanotubes, *ACS Nano*, 2016, **10**, 11317–11326.

36 X. X. Lan, J. Cui, X. F. Zhang, R. Z. Hu, L. Tan, J. Y. He, H. P. Zhang, X. Y. Xiong, X. F. Yang, S. Q. Wu and M. Zhu, Boosting eeversibility and stability of Li storage in SnO_2-Mo multilayers: introduction of interfacial oxygen redistribution, *Adv. Mater.*, 2022, **34**, 2106366.

37 T. Meng, J. W. Qin, Z. Yang, L. R. Zheng and M. H. Cao, Significantly improved Li-ion diffusion kinetics and reversibility of Li_2O in a MoO_2 anode: the effects of oxygen vacancy-induced local charge distribution and metal catalysis on lithium storage, *J. Mater. Chem. A*, 2019, **7**, 17570–17580.

38 H. Kim, H. Kim, S. Muhammad, J. H. Um, M. Shah, P. J. Yoo and W. S. Yoon, Catalytic effect of reduced graphene oxide on facilitating reversible conversion reaction in SnO_2 for next-generation Li rechargeable batteries, *J. Power Sources*, 2020, **446**, 227321.

39 X. Li, L. Zhang, H. Liu, Q. Li and Y. Hou, Magnetic measurements applied to energy storage, *Adv. Energy Mater.*, 2023, **13**, 2300927.

40 Z. Zhao, W. Ye, F. Zhang, Y. Pan, Z. Zhuo, F. Zou, X. Xu, X. Sang, W. Song, Y. Zhao, H. Li, K. Wang, C. Lin, H. Hu, Q. Li, W. Yang and Q. Li, Revealing the effect of LiOH on forming a SEI using a Co magnetic "probe", *Chem. Sci.*, 2023, **14**, 12219–12230.

41 H. Liu, F. Zou, S. Liao, Y. Pan, Z. Zhao, F. Gu, X. Xu, X. Sang, Y. Han, Z. Bu, L. Qin, Y. Wang, G. Chen, M. Ruan, Q. Li, H. Hu and Q. Li, Reinterpreting the intercalation-conversion mechanism of FeP anodes in lithium/sodium-ion batteries from evolution of the magnetic phase, *J. Phys. Chem. Lett.*, 2024, **15**, 4694–4704.

42 F. C. Gu, L. Q. Zhang, Z. H. Li, J. Zhang, Y. Y. Pan, Q. H. Li, H. S. Li, Y. F. Qin and Q. Li, A comparative study of electrochemical and electrostatic doping modulation of magnetism in Fe_3O_4 via ultracapacitor structure, *J. Phys.: Condens. Matter*, 2022, **34**, 455802.

43 Z. H. Li, Y. C. Zhang, X. K. Li, F. C. Gu, L. Q. Zhang, H. J. Liu, Q. T. Xia, Q. H. Li, W. N. Ye, C. Ge, H. S. Li, H. Hu, S. D. Li, Y. Z. Long, S. S. Yan, G. X. Miao and Q. Li, Reacquainting the electrochemical conversion mechanism of FeS_2 sodium-ion batteries by operando magnetometry, *J. Am. Chem. Soc.*, 2021, **143**, 12800–12808.

44 Q. Li, H. S. Li, Q. T. Xia, Z. Q. Hu, Y. Zhu, S. S. Yan, C. Ge, Q. H. Zhang, X. X. Wang, X. T. Shang, S. T. Fan, Y. Z. Long, L. Gu, G. X. Miao, G. H. Yu and J. S. Moodera, Extra storage capacity in transition metal oxide lithium-ion batteries revealed by in situ magnetometry, *Nat. Mater.*, 2021, **20**, 76–83.

45 F. L. Zhang, Z. H. Li, Q. T. Xia, Q. H. Zhang, C. Ge, Y. X. Chen, X. K. Li, L. Q. Zhang, K. Wang, H. S. Li, L. Gu, S. S. Yan, G. X. Miao and Q. Li, Li-ionic control of magnetism through spin capacitance and conversion, *Matter*, 2021, **4**, 3605–3620.

46 X. K. Li, J. Su, Z. H. Li, Z. Q. Zhao, F. L. Zhang, L. Q. Zhang, W. N. Ye, Q. H. Li, K. Wang, X. Wang, H. S. Li, H. Hu, S. S. Yan, G. X. Miao and Q. Li, Revealing interfacial space charge storage of $Li^+/Na^+/K^+$ by operando magnetometry, *Sci. Bull.*, 2022, **67**, 1145–1153.

47 H. S. Li, Z. Q. Hu, Q. T. Xia, H. Zhang, Z. H. Li, H. Z. Wang, X. K. Li, F. K. Zuo, F. L. Zhang, X. X. Wang, W. N. Ye, Q. H. Li, Y. Z. Long, Q. Li, S. S. Yan, X. S. Liu, X. G. Zhang, G. H. Yu and G. X. Miao, Operando magnetometry probing the charge storage mechanism of CoO lithium-ion batteries, *Adv. Mater.*, 2021, **33**, 2006629.

48 S. Fang, D. Bresser and S. Passerini, Transition metal oxide anodes for electrochemical energy storage in lithium- and sodium-ion batteries, *Adv. Energy Mater.*, 2020, **10**, 1902485.

49 S. Y. Lee, K. Y. Park, W. S. Kim, S. Yoon, S. H. Hong, K. Kang and M. Kim, Unveiling origin of additional capacity of SnO_2 anode in lithium-ion batteries by realistic ex situ TEM analysis, *Nano Energy*, 2016, **19**, 234–245.

50 X. S. Zhou, L. J. Wan and Y. G. Guo, Binding SnO_2 nanocrystals in nitrogen-doped graphene sheets as anode materials for lithium-ion batteries, *Adv. Mater.*, 2013, **25**, 2152–2157.

51 T. Wu, Y. H. Cui, K. Y. Wei, C. Z. Lai, Y. Zhao, S. Ni, Y. J. Chen, X. Gao, Y. X. Cui and C. L. Li, Catalysis of nickel nanodomains on Li-F dissociation for high-capacity fluoride cathodes with prior delithiation ability, *Nano Energy*, 2022, **103**, 107843.

52 W. Dong, J. Xu, C. Wang, Y. Lu, X. Liu, X. Wang, X. Yuan, Z. Wang, T. Lin, M. Sui, I. W. Chen and F. Huang, A robust and conductive black tin oxide nanostructure makes efficient lithium-ion batteries possible, *Adv. Mater.*, 2017, **29**, 1700136.

53 C. Hu, L. Chen, Y. J. Hu, A. P. Chen, L. Chen, H. Jiang and C. Z. Li, Optimizing SnO_{2-x}/Fe_2O_3 hetero-nanocrystals toward rapid and highly reversible lithium storage, *Small*, 2021, **17**, 2103532.

54 Q. Y. Xia, F. Zan, Q. Y. Zhang, W. Liu, Q. C. H. Li, Y. He, J. Y. Hua, J. H. Liu, J. Xu, J. S. Wang, C. Z. Wu and H. Xia, All-solid-state thin film lithium/lithium-ion microbatteries for powering the internet of things, *Adv. Mater.*, 2023, **35**, 2200538.

55 S. H. Zheng, H. Wang, P. Das, Y. Zhang, Y. X. Cao, J. X. Ma, S. Z. Liu and Z. S. Wu, Multitasking MXene inks enable high-performance printable microelectrochemical energy storage devices for all-flexible self-powered integrated systems, *Adv. Mater.*, 2021, **33**, 2005449.

© 2025 The Author(s). Published by the Royal Society of Chemistry